Printable Nanostructured Silicon Solar Cells for High-Performance, Large-Area Flexible Photovoltaics

Sung-Min Lee,[†] Roshni Biswas,[‡] Weigu Li,[†] Dongseok Kang,[†] Lesley Chan,[†] and Jongseung Yoon*[,†,‡]

[†]Department of Chemical Engineering and Materials Science and [‡]Department of Electrical Engineering, University of Southern California, Los Angeles, California 90089, United States

ABSTRACT Nanostructured forms of crystalline silicon represent an attractive materials building block for photovoltaics due to their potential benefits to significantly reduce the consumption of active materials, relax the requirement of materials purity for high performance, and hence achieve greatly improved levelized cost of energy. Despite successful demonstrations for their concepts over the past decade, however, the practical application of nanostructured silicon solar cells for large-scale implementation has been hampered by many existing challenges associated with the consumption of the entire wafer or expensive source materials, difficulties to precisely control materials properties and doping characteristics, or restrictions on substrate materials and scalability. Here we present a highly integrable materials platform of nanostructured silicon solar cells that can overcome these limitations. Ultrathin silicon solar microcells integrated with engineered photonic nanostructures are fabricated directly from wafer-based source materials in configurations that can lower the materials cost and can be compatible with deterministic assembly procedures to allow programmable, large-scale distribution, unlimited choices of module substrates, as well as lightweight, mechanically compliant constructions. Systematic studies on optical and electrical properties, photovoltaic performance in experiments, as well as numerical modeling elucidate important design rules for nanoscale photon management with ultrathin, nanostructured silicon solar cells and their interconnected, mechanically flexible modules, where we demonstrate 12.4% solar-to-electric energy conversion efficiency for printed ultrathin (~8 μm) nanostructured silicon solar cells when configured with near-optimal designs of rear-surface nanoposts, antireflection coating, and back-surface reflector.

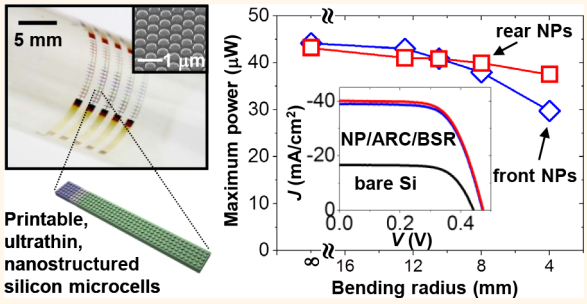

KEYWORDS: ultrathin silicon · nanostructured solar cells · flexible optoelectronics · transfer printing · nanoimprint lithography · nanophotonic light trapping

Crystalline silicon has retained a dominant position as an active material of choice in photovoltaics due to many intrinsic advantages including high natural abundance, nearly ideal band gap, excellent materials safety and reliability, as well as established scientific and engineering infrastructures for manufacturing.[1−3] Despite such favorable attributes, large-scale deployment of this technology demands further decrease in its levelized cost of energy, where the production of high-purity wafer materials is responsible for nearly 50% of the cell fabrication cost.[4] While reducing the thickness of silicon is a conceptually straightforward route to lower the cost of silicon solar cells, it is also accompanied by the degradation of their performance associated with weak optical absorption of silicon for longer wavelength photons.[5] Therefore, approaches to maximize absorption of the solar spectrum in optically thin active materials have been of primary research interest in silicon photovoltaics, aiming to enhance the cost-effectiveness without compromising their photovoltaic performance.[6] In this regard, micro/nanowires or pillars (for small aspect ratios) are a promising class of materials for silicon solar cells as they can offer numerous conceivable advantages including significantly reduced materials consumption, excellent light trapping and absorption enhancement, efficient carrier transport, and ability to use low-purity materials.[7,8] Over the past years, many researchers have studied solar cells based on silicon micro/nanowires fabricated from various "bottom-up" and

* Address correspondence to js.yoon@usc.edu.

Received for review July 15, 2014 and accepted September 25, 2014.

Published online October 01, 2014
10.1021/nn503884z

"top-down" approaches. Silicon micro/nanowires grown by vapor–liquid–solid processes have been successfully demonstrated as pn-junction solar cells as well as photocatalytic electrodes in solar-driven water splitting.[9−11] In top-down approaches, various patterning processes including photolithography,[12] nanoimprint lithography,[13−16] interference lithography,[17] nanosphere lithography,[18,19] and others[20−23] formed micro/nanoscale patterns that can serve as an etch mask for subsequent dry or wet etching of silicon to yield micro/nanowires (or pillars) on wafer-based source materials. The resulting micro/nanostructured solar cells granted many attractive features compared with bottom-up-grown systems such as the use of high-quality wafer materials, ability to precisely tune nanostructured geometries and doping characteristics, as well as absence of residual metallic impurities or crystalline defects. One of most recent advances in this context includes ultrathin monocrystalline silicon solar cells that incorporate subwavelength surface relief and antireflection coating (ARC), where soft-imprint lithography and dry etching were performed on silicon solar cells after the printing to implement light trapping nanostructures.[13,15] Although successfully demonstrated for their concepts, these top-down fabricated solar cells often involve the consumption of the entire wafer,[12,14,24] use of expensive source materials (*e.g.*, silicon-on-insulator wafers),[18,21] or limitations in the choice of substrate materials and scalability,[13,15] thereby frustrating their practical application into cost-effective, large-scale implementation. In the present study, we report a highly integrable, versatile materials platform for nanostructured silicon solar cells that addresses many of these challenges and can be exploited to build high-performance mechanically flexible solar modules. Ultrathin (∼8 μm) monocrystalline silicon solar microcells incorporating engineered photonic nanostructures are fabricated directly from commodity wafer materials as solid-state "ink" elements in configurations that can attain lower materials cost by multiple generations of cell fabrication and can also be integrated with printing-based assembly techniques to allow programmable distribution over large-area, unlimited choices of module substrates, as well as thin, lightweight, and flexible constructions. Optical and electrical properties and photovoltaic performance of resulting nanostructured silicon microcells and their interconnected modules are systematically studied in experiments as well as three-dimensional optical modeling based on finite-difference time-domain (FDTD) methods to elucidate design criteria for nanoscale photon management with ultrathin, nanostructured silicon solar cells in the context of realizing high-performance flexible photovoltaics.

RESULTS AND DISCUSSION

Figure 1a schematically depicts the major steps of fabrication processes for "printable" ultrathin nanostructured silicon solar cells. The process begins with the formation of polymeric mask patterns on a p-type (111) silicon wafer to yield hexagonally periodic nanoscale holes by soft-imprint lithography and oxygen reactive ion etching (RIE), followed by electron beam evaporation and liftoff of Cr (∼7 nm) (Supporting Information Figure S1). The Cr islands were lithographically patterned and used as a mask for inductively coupled plasma reactive ion etching (ICP-RIE) to form arrays of hexagonally packed nanoposts (NPs) on the silicon wafer. The resulting nanostructured silicon served as a starting material for the successive fabrication of ultrathin solar microcells, wherein adapted schemes of previously reported microcell fabrication were employed.[25,26] Briefly, photolithography and ICP-RIE defined vertical trenches to form a bar-shaped microcell layout (∼1000 × 50 μm^2). Subsequently, doping performed by thermal diffusion of solid-state boron and phosphorus source materials implemented electrical contacts as well as a pn-junction on the surface of nanostructured silicon. After the doping over the front surface of microcells, silicon nitride was deposited by plasma-enhanced chemical vapor deposition (PECVD) followed by photolithography and RIE to selectively open the bottom surface of the trench where the anisotropic wet chemical etching can be initiated. Immersion in hot, concentrated KOH solution (∼100 °C) etched through the width of the microcells such that ultrathin, nanostructured bars of the microcells are isolated from the source wafer except for "anchor" regions that remain tethered at both ends of the cell (Figure S2). The fabrication of nanostructured silicon solar cells was completed by doping the exposed bottom surface of microcells to form a back-surface field (BSF) as a minority carrier mirror. Figure 1b,c shows tilted-view scanning electron microscope (SEM) images of lithographically patterned nanoscale Cr islands and an array of ultrathin silicon microcells incorporating periodic surface nanostructures completed on the source wafer, respectively. An entire or selective set of fully functional, nanostructured silicon microcells can be retrieved using an elastomeric stamp with a flat surface or microscale relief features and assembled over a thin sheet of polyethylene terephthalate (PET) in dense (Figure 1d) or sparse (Figure 1e) arrays, respectively, where angle-dependent diffractive colors from the nanostructured surface of the microcells are evidently shown in both configurations.

Optimal designs of subwavelength photonic nanostructures to maximize optical absorption of printed silicon microcells were systematically studied by numerical modeling based on a full-wave, three-dimensional FDTD method. In the present study, we considered two distinct configurations of nanostructured silicon microcells printed on optically transparent polymeric substrates, where hexagonally periodic NPs were

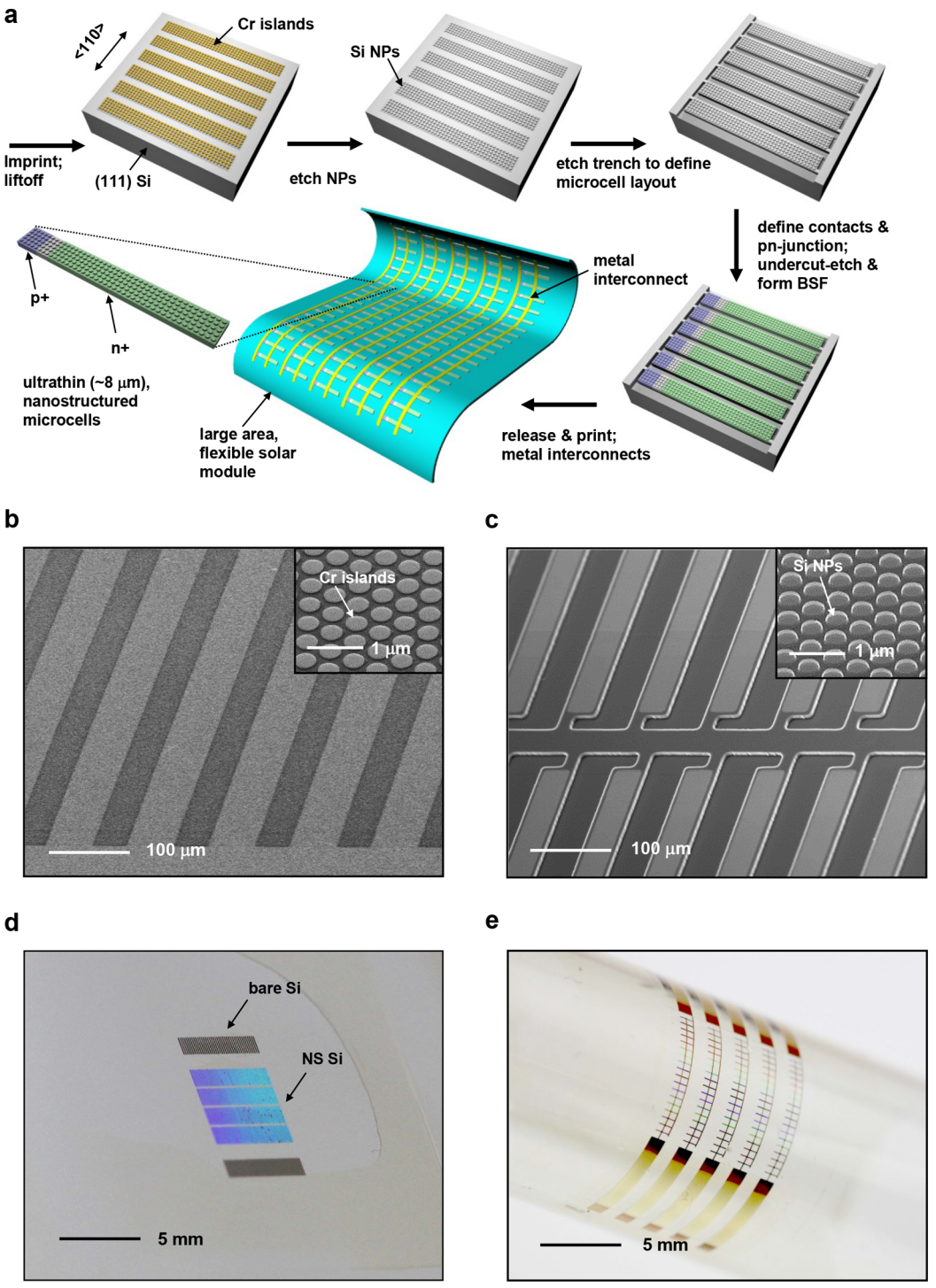

Figure 1. Schematic illustration, SEM, and photographic images of ultrathin, nanostructured silicon microcells and interconnected modules. (a) Schematic illustration of fabrication steps for ultrathin (~8 μm), nanostructured silicon solar microcells derived directly from bulk wafer materials as solid-state ink elements for the deterministic, large-scale assembly to form large-area, flexible solar modules. Tilted-view SEM images of (b) hexagonal arrays of Cr islands on a p-type (111) silicon wafer produced from soft-imprint lithography and liftoff, and (c) completed, ultrathin nanostructured silicon microcells in "printable" forms on the source wafer. Photographic images of (d) densely assembled nanostructured silicon microcells on a PET substrate, and (e) large-area, flexible solar modules composed of sparse arrays of interconnected microcells bent on a cylindrical support with a diameter of ~12 mm, where angle-dependent diffractive colors are evidently shown in both cases.

placed either on front- or rear-surfaces of microcells with respect to the position of an illumination source. The configuration for rear-surface NPs is a particularly interesting option to consider as it can provide advantages of eliminating shadowing losses associated with metal interconnects and also reducing the angular dependence of photovoltaic performance compared to cells with NPs on their front-surface, as

described in detail subsequently. After the transfer printing, the nanostructured surface of microcells is exposed to the air on the module substrate, where the position of the light source defines the configuration of the printed microcells. Accordingly, microcells with rear-surface NPs are realized by illuminating through the bottom surface of a transparent substrate such that the light is incident on a flat surface of microcells. A series of FDTD calculations were systematically performed over the entire space of design parameters including period (p), diameter (D), and height (h) of NPs at normal incidence of light, from which reflection (R), transmission (T), and absorption (A) spectra can be obtained. To quantitatively evaluate the enhancement of photon absorption in nanostructured silicon against solar illumination, calculated absorption was integrated over the AM1.5G standard solar spectrum to yield integrated solar flux absorption,[20] S_abs, given by eq 1:

$$S\_abs = \frac{\int_{400}^{1100} \frac{\lambda}{hc} A(\lambda) I_{1.5G}(\lambda) d\lambda}{\int_{400}^{1100} \frac{\lambda}{hc} I_{1.5G}(\lambda) d\lambda} \quad (1)$$

where h, c, and $I_{1.5G}$ are Planck's constant, speed of light, and the standard solar irradiance (AM 1.5G; ASTM G-173), respectively. Figure 2a shows a contour plot of such calculated integrated solar flux absorption for ultrathin (8 μm) silicon with front-surface NPs as a function of diameter and height of NPs at a fixed NP period (400 nm), where air (n = 1.0) and polymer (n = 1.56) constitute a semi-infinite medium above and below the printed microcells, respectively. Accordingly, the maximum integrated absorption with corresponding NP's diameter and height can be determined at each NP period (*e.g.*, D = 280 nm, h = 130 nm at p = 400 nm, Figures S3 and S4). Starting from microcells that only have NPs, we also examined cell configurations that additionally incorporate a single-layer ARC, a specular back-side reflector (BSR), or both ARC and BSR. Figure 2b summarizes maximum values of integrated solar flux absorption as a function of NP period in respective cell configurations. As expected, the optimum period of NPs varies with the cell configuration, which are 400, 500, 400, and 700 nm for microcells that have NPs, NPs with ARC, NPs with BSR, and NPs with both ARC and BSR, and corresponding maximum integrated absorptions are 79.7, 83.6, 85.5, and 91.1%, respectively. The thicknesses of ARC (TiO_2, n = 2.5) optimized to maximize the integrated absorption at optimum geometries of NPs are ~60 nm for periods of 500 to 1000 nm, ~50 nm for a period of 400 nm, and ~40 nm for a period of 300 nm. Adding the ARC (blue diamonds in Figure 2b) at smaller NP periods (*e.g.*, 300 and 400 nm) is less significant to further improve the absorption, where the antireflection effect from NPs is already strong. The absorption enhancement from ARC is comparatively stronger at larger NP periods, as the antireflection band from the NPs is red-shifted and hence the additional ARC can effectively compensate for reflection losses in the shorter wavelength range of high solar irradiance. The BSR (green diamonds) was effective to improve the absorption in all NP periods due to the weak optical absorption of ultrathin silicon for longer wavelength photons, while the maximum enhancement occurred at smaller NP periods where the antireflection effect from NPs for shorter wavelength photons is synergistically combined with the BSR effect for longer wavelength photons. Notably, the highest system performance is obtained when both ARC and BSR are implemented in a complementary way (orange diamonds), where the maximum integrated absorption occurs at the NP period of 700 nm, with little variation of performance over different NP periods. Corresponding reflection and absorption spectra for the maximum integrated absorption at each microcell configuration (Figures 2c,d and S5−S8) also support the above discussion. Figure 2e presents log-scale contour plots of absorbed power of ultrathin bare silicon (top row), silicon with NPs (middle row), and with NPs, ARC, and BSR (bottom row) at optimal NP geometries for each configuration and wavelengths of 400, 600, 800, and 1000 nm, respectively. Consistent with previous studies,[13,15] having the front-surface NPs can significantly improve the absorption throughout the entire wavelength range by the combined effects of antireflection, diffraction, and light trapping. The additional ARC and BSR further boost the absorption effectively in shorter and longer wavelength photons, respectively. Using calculated reflection and absorption spectra, normalized absorption, $A/(1 - R)$, can be also extracted, which provides the fraction of absorbed photons among those that enter the ultrathin silicon and therefore can evaluate the effectiveness of light trapping (Figure 2f). The normalized absorption in bare silicon (blue line) begins to decrease significantly for wavelengths greater than 600 nm due to the weak absorption of ultrathin silicon, which is where significant levels of improvement can be made by implementing front-surface NPs (red line).

We also considered an alternative configuration of printed nanostructured microcells, where NPs are located at their rear-surface with respect to the light source, and thus shadowing losses associated with metal interconnects can be eliminated. FDTD calculations were performed in a similar fashion to microcells with front-surface NPs but with modified illumination conditions, where the light is incident on the flat surface of silicon through a polymeric medium, with a corrected solar irradiance to consider the reflection loss (~4%) at the substrate (*e.g.*, polymer)−air interface. Figure 3a shows a contour plot of integrated solar flux absorption for ultrathin (8 μm) silicon with rear-surface NPs at the NP period of 700 nm, wherein the NP

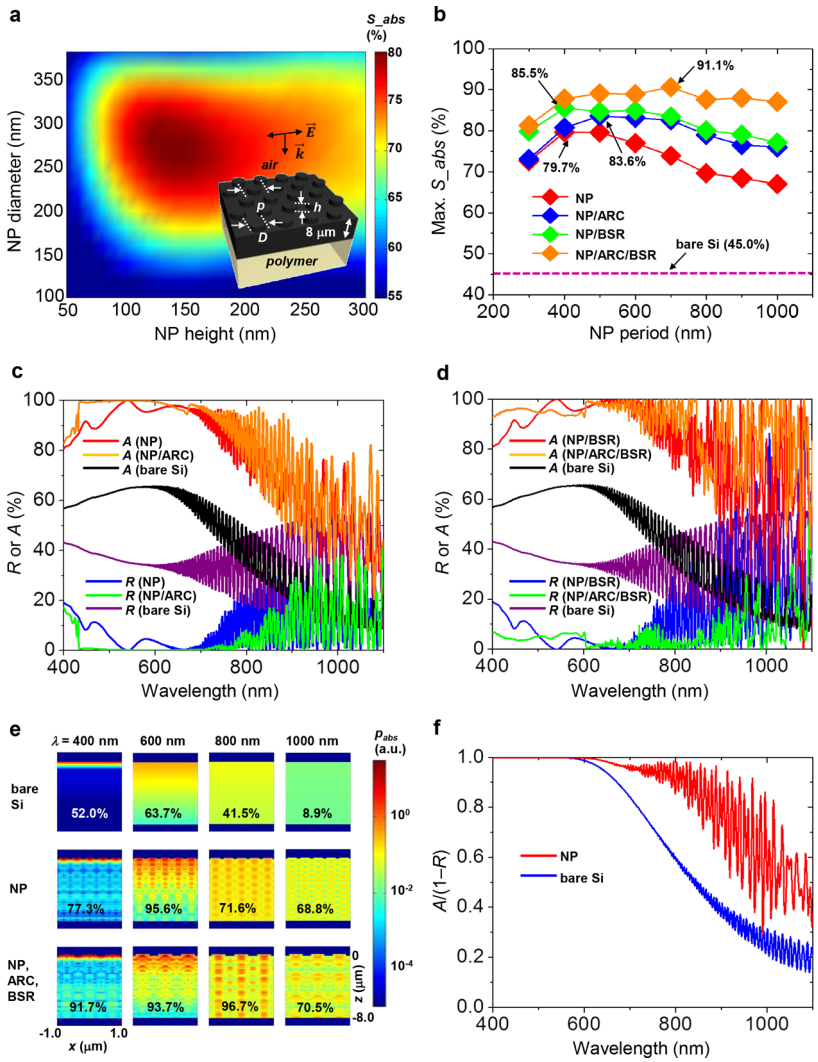

Figure 2. Numerical modeling of optical properties for ultrathin silicon with front-surface NPs. (a) Contour plot of the integrated solar flux absorption (*S_abs*) for ultrathin (8 μm) silicon with front-surface NPs as a function of diameter (*D*) and height (*h*) of the NP at the period of 400 nm. Inset schematically illustrates the configuration for FDTD calculations, where the light is normally incident on the nanostructured surface of silicon printed on a polymeric medium (n = 1.56). (b) Maximum integrated solar flux absorption of ultrathin silicon as a function of NP period at various cell configurations including silicon that incorporates NPs, NPs with ARC, NPs with BSR, and NPs with both ARC and BSR. Corresponding reflection (*R*) and absorption (*A*) spectra that yield maximum integrated solar flux absorption of ultrathin silicon that incorporates (c) NPs and NPs with ARC, and (d) NPs with BSR and NPs with both ARC and BSR. (e) Log-scale contour plots of absorbed power per unit volume for ultrathin bare silicon (top row), silicon with NPs (middle row), and silicon with NPs, ARC, and BSR (bottom row) at optimal NP geometries of each configuration and wavelengths of 400, 600, 800, and 1000 nm. (f) Normalized absorption spectra, $A/(1-R)$, of ultrathin silicon with and without front-surface NPs.

geometry of highest performance can be extracted (*e.g.*, D = 560 nm, h = 200 nm at p = 700 nm, Figures S9 and S10). As illustrated in Figure 3b−d, the maximum performance of microcells was obtained at NP periods of 700, 500, 700, and 500 nm for microcells that incorporate NPs, NPs with ARC, NPs with BSR, and NPs with both ARC and BSR, respectively, where corresponding maximum integrated solar flux absorption are 72.1, 83.5, 75.9, and 87.7% (Figures S11−S14). The same optimal thickness (t = 60 nm) of TiO_2 (n = 2.50) was applied as an ARC in all NP periods, while a layer of polymer (t = 6 μm, n = 1.56) was added between the nanostructured surface and a silver BSR to eliminate ohmic losses. NPs implemented on the rear surface of microcells mainly act as a diffraction grating that redirects longer wavelength photons that are not absorbed effectively by optically thin silicon. Consequently, the enhancement from the BSR is relatively limited compared with that in bare silicon or silicon with front-surface NPs, as the majority of longer wavelength photons are already diffracted back to the silicon by rear-surface NPs. Implementing the ARC on the flat surface of microcells is equally effective at all NP periods to increase the absorption for shorter wavelength photons. Notably, the absorption of microcells with rear-surface NPs becomes comparable to those with front-surface NPs with the addition of ARC or both ARC and BSR, suggesting that it can be even higher if

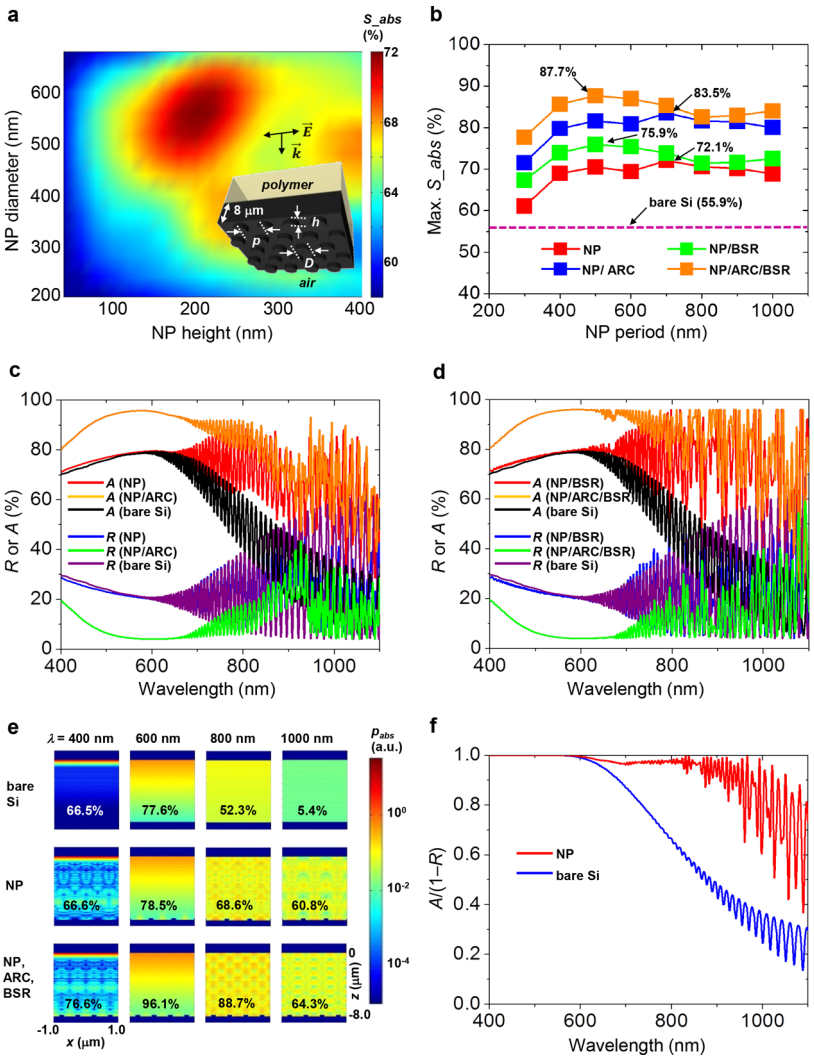

Figure 3. Numerical modeling of optical properties for ultrathin silicon with rear-surface NPs. (a) Contour plot of the integrated solar flux absorption for ultrathin (8 μm) silicon with rear-surface NPs as a function of diameter (*D*) and height (*h*) of the NP at the period of 700 nm. Inset schematically illustrates the configuration for FDTD calculations, where light is normally incident on a substrate and through a flat surface of nanostructured silicon. (b) Maximum integrated solar flux absorption of ultrathin silicon as a function of NP period at various cell configurations including silicon that incorporates NPs, NPs with ARC, NPs with a specular BSR, and NPs with both ARC and BSR. Corresponding reflection (*R*) and absorption (*A*) spectra that yield maximum integrated solar flux absorption of ultrathin silicon that incorporates (c) NPs and NPs with ARC, and (d) NPs with BSR and NPs with both ARC and BSR. (e) Log-scale contour plots of absorbed power per unit volume for ultrathin bare silicon (top row), silicon with NPs (middle row), and silicon with NPs, ARC, and BSR (bottom row) at optimal geometries of each configuration and wavelengths of 400, 600, 800, and 1000 nm, respectively. (f) Normalized absorption spectra, $A/(1-R)$, of ultrathin silicon with and without rear-surface NPs.

the effect of eliminating shadowing losses is included. The effectiveness of rear-surface NPs to enhance the absorption for longer wavelength photons, as well as synergistic benefits of having both ARC and BSR, is clearly appreciable in the log-scale contour plots (Figure 3e) of absorbed power for bare silicon (top row), silicon with NPs (middle row), and with NPs, ARC, and BSR (bottom row). It is also noteworthy that the light trapping for longer wavelength photons is comparatively more effective in microcells with rear-surface NPs than those with front-surface NPs as depicted in Figure 3f.

On the basis of theoretical consideration of optical properties, we fabricated ultrathin (~8 μm) silicon microcells with near-optimal NP geometries, where the period of ~500 nm ($D \approx 350$ nm, $h \approx 140$ nm) was employed for microcells with both configurations of NPs. Following procedures described earlier, completed microcells were released from the source wafer and printed on a glass (~1 mm) and PET (~50 μm) substrate coated with a thin (~30 μm) layer of transparent, photocurable polymer (NOA61), followed by optical and electrical characterizations of individual microcells and interconnected modules. Figure 4a,b presents experimentally measured (thick line) reflection (red, blue) and absorption (orange, green) spectra of ultrathin silicon microcells printed on a glass substrate, with front- and rear-surface NPs and with NPs

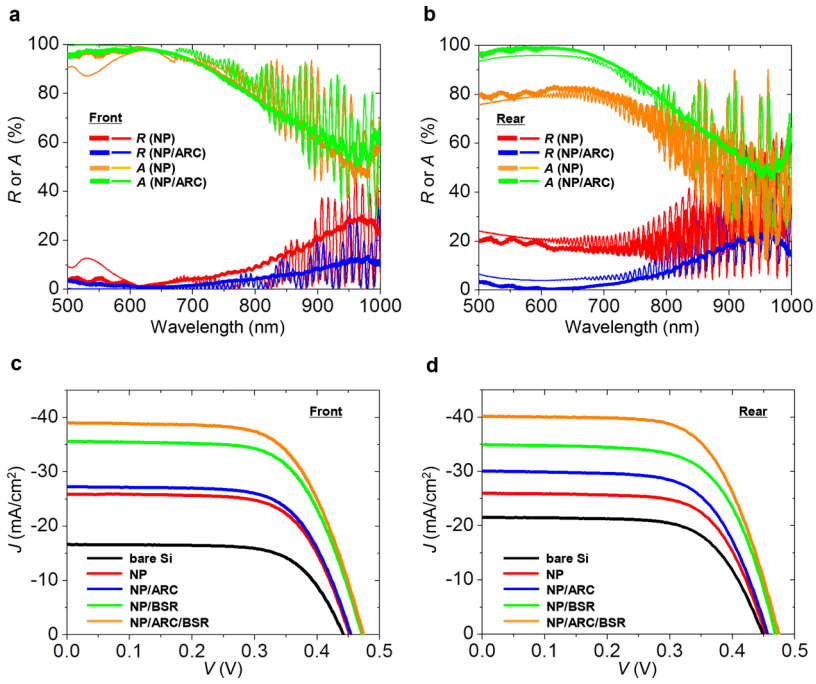

Figure 4. Measured optical and photovoltaic characteristics of printed nanostructured microcells. Measured (thick line) reflection (red, blue) and absorption (orange, green) spectra of ultrathin silicon microcells printed on a glass substrate, which incorporate (a) front- and (b) rear-surface NPs (p = 500 nm, D = 350 nm, h = 140 nm), and NPs with ARC (TiO_2, n = 2.50, t = 60 nm), respectively, where calculated spectra (thin line) with the same NP geometries as measurements are also included. Corresponding representative J–V curves of individual microcells with (c) front- and (d) rear-surface NPs at various cell configurations obtained under AM 1.5G standard solar illumination.

and ARC (TiO_2, $t \approx 60$ nm, $n = 2.50$ at 633 nm), respectively, where thin lines correspond to the calculated spectra for silicon with the same NP geometries as in experiments. Measurements of reflection and transmission spectra were performed in optical configurations that match closely with the simulation. For microcells with front-surface NPs, a white illumination source was focused through an objective lens (50×, NA = 0.42) on a circular area (diameter ~20 μm) of the nanostructured surface, where the reflected or transmitted light was collected back to the same or secondary (20×, NA = 0.40) objective lens and guided to a fiber-optic-coupled spectrometer (Figure S15). For microcells with rear-surface NPs, the illumination source was incident through a glass substrate and the polymer layer and focused on the flat surface of microcells. A silver mirror and a glass substrate coated with the printing medium were employed as a 100% calibration standard for reflection and transmission, respectively. Both experimentally measured reflection and absorption ($A = 1 - R - T$) spectra were in good agreement with the calculation under the same optical configurations. Corresponding photovoltaic performance of nanostructured silicon microcells was obtained under the simulated AM1.5G standard solar spectrum (1000 W/m^2) at room temperature. Figure 4c,d depicts representative current density (J)–voltage (V) curves of individual microcells that have front- and rear-surface NPs, NPs with ARC, NPs with BSR, and NPs with both BSR and ARC. The overall trend of performance increase at each device configuration is quantitatively consistent with the calculation, where the observed enhancement in short-circuit current density (J_{sc}) matched well with the calculated improvement in the integrated solar flux absorption (S_abs). For microcells with front-surface NPs, short-circuit current densities were 16.6, 26.1, 27.3, 35.6, and 39.0 mA/cm^2, open-circuit voltages (V_{oc}) were 444, 451, 453, 472, and 473 mV, and solar-to-electric energy conversion efficiencies (η) were 5.1, 8.0, 8.3, 11.0, and 12.0%, respectively, for bare silicon microcells, microcells that have NPs, NPs with ARC, NPs with BSR, and NPs with both ARC and BSR. For microcells with rear-surface NPs, corresponding values of short-circuit current densities were 21.5, 26.0, 30.1, 34.9, and 40.1 mA/cm^2, open-circuit voltages were 448, 452, 456, 467, and 473 mV, efficiencies were 6.4, 7.9, 8.9, 10.7, and 12.4%, respectively. The efficiency of 8 μm thick microcells that have front-surface NPs, NPs with ARC, NPs with BSR, and NPs with both ARC and BSR increased by 57.7, 63.0, 117.2, and 137.5% compared with the efficiency of bare silicon microcells without NP implementation, with corresponding enhancement for microcells with rear-surface NPs of 22.7, 39.0, 66.6, and 92.2%, respectively. More details for measured characteristics of photovoltaic performance appear in the Supporting Information (Figure S16, Table S1). The enhancement with BSR in both cases also includes contributions from photons

that are incident outside the cell area and guided through polymeric printing medium and a glass substrate. Notably, microcells with rear-surface NPs, due to the elimination of shadowing losses (~9.2% of the top surface area) associated with metal interconnects, exhibited comparable performance to those with front-surface NPs even though NP geometries are not fully optimized. It is also noteworthy that the relative contribution of each light management scheme (*i.e.*, NPs, ARC, BSR) varies with the thickness of silicon (Figure S17). The effectiveness of BSR gradually decreases upon the increase of silicon thickness as the less amount of photons reaches the BSR with the increased optical path length and absorption. Consequently, the integrated absorption for microcells that incorporate NPs becomes comparable to microcells with NPs and BSR at larger silicon thicknesses, while the highest performance was obtained from microcells that have both NPs and ARC (or ARC and BSR) in the "optically thick" regime. Similar trends were observed for microcells with rear-surface NPs. The computational model also suggests that the integrated absorption sharply increases at silicon thicknesses lower than ~10 μm for all optical configurations, while the rate of increase substantially diminishes at a larger thickness of silicon.

Angular dependence of photovoltaic performance is a critically important design factor for the practical application of nanostructured silicon solar cells in flexible solar modules, where the incidence angle of solar radiation is not always uniformly normal to the surface of solar cells due to the inherent curvature of module substrates. Moreover, as in all diffraction-based optical elements, optical properties of nanostructured silicon are highly sensitive to the incidence angle of illumination. To further elucidate this effect in the reported system, we examined the angular dependence of photovoltaic performance of ultrathin, nanostructured silicon microcells and their interconnected modules in both experiments and numerical modeling. Figure 5a presents calculated integrated solar flux absorption of ultrathin, nanostructured silicon that incorporates front- and rear-surface NPs and NPs with ARC as a function of incidence angle (θ) of illumination, in which optimal NP geometries at each cell configuration were used, and the calculated absorption was averaged over both transverse electric and transverse magnetic polarizations (Figure S18). It is clearly shown that the integrated solar flux absorption of silicon degrades more steeply for microcells with front-surface NPs, which is consistent with the trend of the measured maximum power of an individual microcell under AM1.5G standard solar illumination as depicted in Figure 5b. Such angular dependence of individual microcells also translates into the performance of mechanically bendable modules. Figure 5c shows the maximum output power ("open" points) of a solar

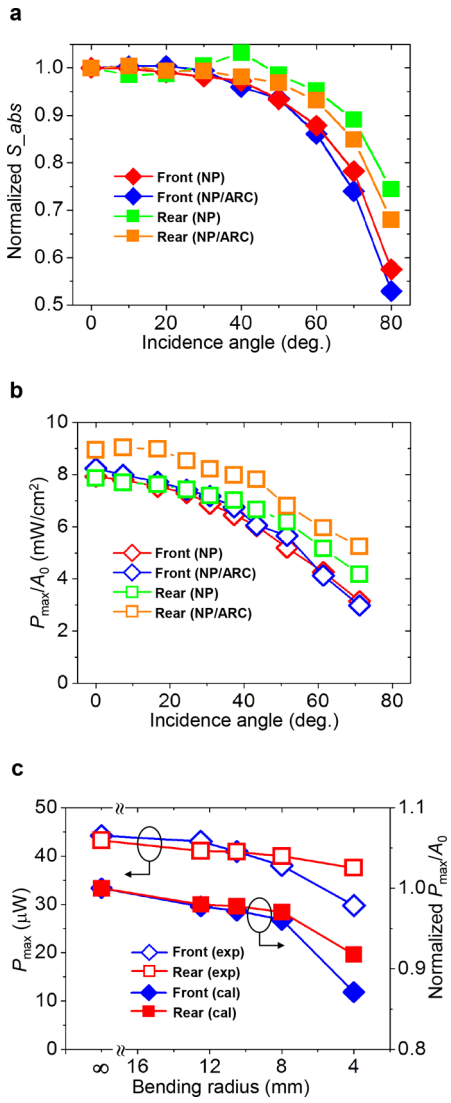

Figure 5. Angular dependence of photovoltaic performance of individual microcells and interconnected modules. (a) Normalized integrated solar flux absorption of ultrathin, nanostructured silicon incorporating front- and rear-surface NPs and NPs with ARC as a function of incidence angle of AM1.5G solar illumination, where the optimal NP design at each microcell configuration was used for calculation, and normalization was performed by the data at normal incidence. (b) Measured maximum power density (normalized over the cell area) of individual nanostructured microcells that have the same NP geometry as in Figure 4, as a function of incidence angle of illumination. (c) Measured maximum power of a mechanically bendable solar module composed of 15 interconnected microcells (cell-to-cell spacing = ~450 μm) that incorporate front- and rear-surface NPs as a function of bending radius, where the microcell at the center of the array was placed to have the illumination at a normal incidence. Calculated maximum power density assumed the same module design but using the individual cell performance obtained from the measurements in (b).

module composed of 15 interconnected microcells at the cell-to-cell spacing of ~450 μm as a function of bending radius. As expected, the performance of flexible modules with rear-surface NPs changes much less sensitively than those with front-surface NPs, which also matched with the variation of normalized

output power ("closed" points) estimated based on the measured angular dependence of individual cell performance (Figure 5b).

CONCLUSION

In summary, we presented a highly versatile materials platform of nanostructured silicon solar cells that can offer significant benefits in cost, device performance, and integration pathways that are unavailable in existing silicon solar cell technologies. Optimal designs of periodic NPs for nanoscale photon management were implemented directly on the source wafer such that ultrathin, nanostructured silicon microcells are generated in printable formats that can allow, in conjunction with deterministic materials assembly, reduced materials cost by multiple generations of cell fabrication, large-area, programmable distribution over unlimited types of module substrates, as well as thin, lightweight, and flexible constructions. Microcells implemented with rear-surface NPs provided advantages due to the elimination of shadowing losses associated with metal interconnects as well as comparatively lower angular dependence of cell performance at oblique incidence angles, where 12.4% solar-to-electric efficiency was demonstrated for printed 8 μm thick microcells configured with rear-surface NPs, ARC, and BSR. The results reported here therefore indicate great promise of this approach for large-scale implementation of nanostructured silicon solar cells, particularly for high-performance flexible photovoltaic modules. The underlying principle can be readily applicable to other silicon-based devices that can benefit from controllable photon management, reduced materials cost, as well as versatile integration possibilities.

METHODS

Fabrication of Ultrathin, Nanostructured Si Solar Microcells and Interconnected Modules. The fabrication of ultrathin, nanostructured silicon microcells began with the formation of polymeric (SU8 2000.5, Microchem) mask patterns on a p-type (111) Czochralski silicon wafer (9−37 Ω·cm, Virginia Semiconductors) to yield hexagonally periodic nanoscale holes by soft-imprint lithography and oxygen reactive ion etching (Plasmalab), followed by electron beam evaporation (Temescal) and liftoff of Cr (~7 nm). The deposited Cr islands were subsequently defined within the boundary of individual microcells by photolithography and wet chemical etching (CR-7, Cyantek) and used as a mask for inductively coupled plasma reactive ion etching (Plasmalab system 100, Oxford) to form arrays of hexagonally packed NPs on the silicon wafer. The resulting nanostructured silicon was used as a starting material for the successive fabrication of ultrathin solar microcells.[25,26] Photolithography and ICP-RIE defined vertical trenches with the depth of ~8 μm to form arrays of microcell layout, where the direction of trench width was aligned to the [110] orientation of silicon to enable the release of ultrathin silicon from the source wafer. Doping by thermal diffusion (1000 °C under N_2 atmosphere) of boron (BN-1250, Saint Gobain) and phosphorus (PH-1000, Saint Gobain) solid-state doping sources implemented electrical contacts as well as the pn-junction on the surface of nanostructured silicon, where silicon nitride (~1.2 μm) deposited by plasma-enhanced chemical vapor deposition (Plasmalab) served as a selective doping mask. Subsequently, silicon nitride (~2 μm) was deposited by PECVD, followed by photolithography and RIE to selectively open the bottom surface of the trench where the wet chemical etching of silicon can be initiated. Immersion in hot (~100 °C) concentrated KOH solution (PSE-200, Transcene) preferentially etched through the width of microcells to allow the bottom surface of nanostructured microcells to be isolated from the source wafer except for "anchor" regions that remain tethered at both ends of the cell. The subsequent p-type doping on the bottom surface of microcells incorporated a back-surface field as a minority carrier mirror. An entire or selective set of completed nanostructured silicon microcells was retrieved using an elastomeric stamp made of polydimethylsiloxane (sylguard 184, Dow Corning) with a flat surface or microstructured relief features and assembled over a thin sheet of polyethylene terephthalate (~50 μm) or on a glass (~1 mm) substrate using a photocurable polyurethane (NOA61, Norland Products). Titanium dioxide (TiO_2) and silver were deposited by RF magnetron sputtering (Orion 5, AJA International) as a single-layer antireflection coating and by an electron beam evaporator as a BSR, respectively. A thin (~20 μm) layer of SU8 was spin-coated on the nanostructured surface of printed microcells before depositing silver as BSR for microcells with rear-surface NPs. For the flexible modules, metals (Cr/Ag/Au = 15/1000/20 nm) were deposited on printed microcells by electron beam evaporation, followed by spin-coating of a polymeric encapsulation layer (SU8 2005, Microchem) to implement schemes of a neutral mechanical plane. More details of fabrication procedures also appear in the Supporting Information.

Optical and Electrical Characterization of Microcells. Reflection and transmission spectra were measured using a home-made setup comprising a white illumination source and fiber-optic spectrometer (USB 4000, Ocean Optics). A source light coming out of a multimode fiber was collimated using an achromatic doublet lens (f = 19 mm, NA = 0.42) and then focused onto the region of interest in the sample with a beam diameter of ~25 μm through an objective lens (50×, NA = 0.42). The reflected light was collected with the same objective lens and coupled to a multimode fiber using an achromatic fiber-port lens (EFL = 18 mm). For transmission spectra, another objective lens (20×, NA = 0.40) was used for coupling the transmitted light into a multimode fiber through an achromatic doublet lens (f = 25 mm, NA = 0.51). The reflected or transmitted light was fed to the spectrometer recording the spectrum from 500 to 1000 nm. For a 100% calibration standard, a silver mirror and a substrate with a printing medium were used in reflection and transmission measurements, respectively. Current−voltage characteristics were measured using a semiconductor parameter analyzer (4156C, Agilent Technologies) and a full-spectrum solar simulator (94042A, Oriel). A home-built rotation stage was used to evaluate angular dependence of photovoltaic performance of microcells.

Optical Modeling of Nanostructured Microcells. Optical properties of nanostructured silicon microcells were simulated by a finite-difference time-domain method (Lumerical Solutions). For calculations at normal incidence ($\theta = 0°$), a 3D simulation volume was defined with a periodic boundary condition in x- and y-directions and a perfectly matched layers boundary condition in z-direction, with a light source of continuous plane-wave that has a broad Gaussian frequency spectrum (270−750 THz). For oblique incidence cases ($\theta \neq 0°$), a "Bloch" boundary condition was employed in x- and y-directions, with a continuous plane-wave that has a narrow Gaussian frequency spectrum centered at a wavelength of interest. Contour plots of absorbed power per unit volume at specific wavelengths were obtained from calculated electric field profiles based on $p_{abs} = -0.5\omega|\vec{E}|^2 imag(\varepsilon)$, where ω, $\vec{E}$, and ε are angular frequency, electric field, and permittivity of the medium, respectively. The refractive indices

of silicon and silver were obtained from the literature,[27] while those for glass, TiO_2, and polymer were fixed at 1.5, 2.5, and 1.56, respectively, based on values obtained from measurements.

Conflict of Interest: The authors declare no competing financial interest.

Acknowledgment. S.-M.L., W.L., D.K., and J.Y. gratefully thank the National Science Foundation under Grant No. ECCS-1202522 for support. R.B. contributed to the reflection/transmission measurements under support from the Center for Energy Nanoscience, an Energy Frontiers Research Center funded by the U.S. Department of Energy, Office of Science, Office of Basic Energy Sciences, under Award No. DE-SC0001013. The authors acknowledge M. Povinelli at USC for use of the optical characterization setup, A. Armani at USC for use of the ellipsometer, and S. Jeon at KAIST for help on soft-imprint lithography. The authors thank X. Cao for help on cell fabrication, the Center for Energy Nanoscience at USC for the use of the spectrophotometer, Donghai Zhu and John Curulli for help using facilities at Keck photonics laboratory and center for electron microscope and microanalysis (CEMMA) at USC, respectively.

Supporting Information Available: Detailed fabrication steps of nanostructured silicon microcells and flexible solar modules, optical and SEM images, calculated reflectance and absorption spectra, schematics and photographic image of optical measurement setup, and photovoltaic performance characteristics of printed nanostructured microcells. This material is available free of charge *via* the Internet at http://pubs.acs.org.

REFERENCES AND NOTES

1. Ginley, D.; Green, M. A.; Collins, R. Solar Energy Conversion toward 1 Terawatt. *MRS Bull.* **2008**, *33*, 355–364.
2. Bagnall, D. M.; Boreland, M. Photovoltaic Technologies. *Energy Policy* **2008**, *36*, 4390–4396.
3. Wolden, C. A.; Kurtin, J.; Baxter, J. B.; Repins, I.; Shaheen, S. E.; Torvik, J. T.; Rockett, A. A.; Fthenakis, V. M.; Aydil, E. S. Photovoltaic Manufacturing: Present Status, Future Prospects, and Research Needs. *J. Vac. Sci. Technol., A* **2011**, *29*, 030801.
4. Rodriguez, H.; Guerrero, I.; Koch, W.; Endrös, A. L.; Franke, D.; Häßler, C.; Kalejs, J. P.; Möller, H. J. Bulk Crystal Growth and Wafering for PV. In *Handbook of Photovoltaic Science and Engineering*; John Wiley & Sons: New York, 2011; pp 218−264.
5. Shah, A.; Torres, P.; Tscharner, R.; Wyrsch, N.; Keppner, H. Photovoltaic Technology: The Case for Thin-Film Solar Cells. *Science* **1999**, *285*, 692–698.
6. Atwater, H. A.; Polman, A. Plasmonics for Improved Photovoltaic Devices. *Nat. Mater.* **2010**, *9*, 205–213.
7. Mokkapati, S.; Catchpole, K. R. Nanophotonic Light Trapping in Solar Cells. *J. Appl. Phys.* **2012**, *112*, 101101.
8. Brongersma, M. L.; Cui, Y.; Fan, S. H. Light Management for Photovoltaics Using High-Index Nanostructures. *Nat. Mater.* **2014**, *13*, 451–460.
9. Kelzenberg, M. D.; Boettcher, S. W.; Petykiewicz, J. A.; Turner-Evans, D. B.; Putnam, M. C.; Warren, E. L.; Spurgeon, J. M.; Briggs, R. M.; Lewis, N. S.; Atwater, H. A. Enhanced Absorption and Carrier Collection in Si Wire Arrays for Photovoltaic Applications. *Nat. Mater.* **2010**, *9*, 239–244.
10. Kelzenberg, M. D.; Turner-Evans, D. B.; Putnam, M. C.; Boettcher, S. W.; Briggs, R. M.; Baek, J. Y.; Lewis, N. S.; Atwater, H. A. High-Performance Si Microwire Photovoltaics. *Energy Environ. Sci.* **2011**, *4*, 866–871.
11. Adachi, M. M.; Anantram, M. P.; Karim, K. S. Core−Shell Silicon Nanowire Solar Cells. *Sci. Rep.* **2013**, *3*, 1546.
12. Gharghi, M.; Fathi, E.; Kante, B.; Sivoththaman, S.; Zhang, X. Heterojunction Silicon Microwire Solar Cells. *Nano Lett.* **2012**, *12*, 6278–6282.
13. Shir, D.; Yoon, J.; Chanda, D.; Ryu, J.-H.; Rogers, J. A. Performance of Ultrathin Silicon Solar Microcells with Nanostructures of Relief Formed by Soft Imprint Lithography for Broad Band Absorption Enhancement. *Nano Lett.* **2010**, *10*, 3041–3046.
14. Shin, J. C.; Chanda, D.; Chern, W.; Ki Jun, Y.; Rogers, J. A.; Xiuling, L. Experimental Study of Design Parameters in Silicon Micropillar Array Solar Cells Produced by Soft Lithography and Metal-Assisted Chemical Etching. *IEEE J. Photovoltaics* **2012**, *2*, 129–133.
15. Yu, K. J.; Gao, L.; Park, J. S.; Lee, Y. R.; Corcoran, C. J.; Nuzzo, R. G.; Chanda, D.; Rogers, J. A. Light Trapping in Ultrathin Monocrystalline Silicon Solar Cells. *Adv. Energy Mater.* **2013**, *3*, 1401–1406.
16. Mellor, A.; Hauser, H.; Wellens, C.; Benick, J.; Eisenlohr, J.; Peters, M.; Guttowski, A.; Tobias, I.; Marti, A.; Luque, A.; *et al.* Nanoimprinted Diffraction Gratings for Crystalline Silicon Solar Cells: Implementation, Characterization and Simulation. *Opt. Express* **2013**, *21*, A295–A304.
17. Song, Y. M.; Yu, J. S.; Lee, Y. T. Antireflective Submicrometer Gratings on Thin-Film Silicon Solar Cells for Light-Absorption Enhancement. *Opt. Lett.* **2010**, *35*, 276–278.
18. Jeong, S.; McGehee, M. D.; Cui, Y. All-Back-Contact Ultrathin Silicon Nanocone Solar Cells with 13.7% Power Conversion Efficiency. *Nat. Commun.* **2013**, *4*, 2950.
19. Garnett, E.; Yang, P. Light Trapping in Silicon Nanowire Solar Cells. *Nano Lett.* **2010**, *10*, 1082–1087.
20. Chan, L.; Kang, D.; Lee, S.-M.; Li, W.; Hunter, H.; Yoon, J. Broadband Antireflection and Absorption Enhancement of Ultrathin Silicon Solar Microcells Enabled with Density-Graded Surface Nanostructures. *Appl. Phys. Lett.* **2014**, *104*, 223905.
21. Lu, Y. R.; Lal, A. High-Efficiency Ordered Silicon Nanoconical-Frustum Array Solar Cells by Self-Powered Parallel Electron Lithography. *Nano Lett.* **2010**, *10*, 4651–4656.
22. Peng, K. Q.; Xu, Y.; Wu, Y.; Yan, Y. J.; Lee, S. T.; Zhu, J. Aligned Single-Crystalline Si Nanowire Arrays for Photovoltaic Applications. *Small* **2005**, *1*, 1062–1067.
23. Shen, X.; Sun, B.; Liu, D.; Lee, S.-T. Hybrid Heterojunction Solar Cell Based on Organic−Inorganic Silicon Nanowire Array Architecture. *J. Am. Chem. Soc.* **2011**, *133*, 19408–19415.
24. Jeong, S.; Garnett, E. C.; Wang, S.; Yu, Z.; Fan, S.; Brongersma, M. L.; McGehee, M. D.; Cui, Y. Hybrid Silicon Nanocone−Polymer Solar Cells. *Nano Lett.* **2012**, *12*, 2971–2976.
25. Yoon, J.; Baca, A. J.; Park, S.-I.; Elvikis, P.; Geddes, J. B.; Li, L.; Kim, R. H.; Xiao, J.; Wang, S.; Kim, T.-H.; *et al.* Ultrathin Silicon Solar Microcells for Semitransparent, Mechanically Flexible and Microconcentrator Module Designs. *Nat. Mater.* **2008**, *7*, 907–915.
26. Yoon, J.; Li, L.; Semichaevsky, A. V.; Ryu, J. H.; Johnson, H. T.; Nuzzo, R. G.; Rogers, J. A. Flexible Concentrator Photovoltaics Based on Microscale Silicon Solar Cells Embedded in Luminescent Waveguides. *Nat. Commun.* **2011**, *2*, 343.
27. Palik, E. D. *Handbook of Optical Constants of Solids*; Academic Press: London, 1998; Vol. 3.